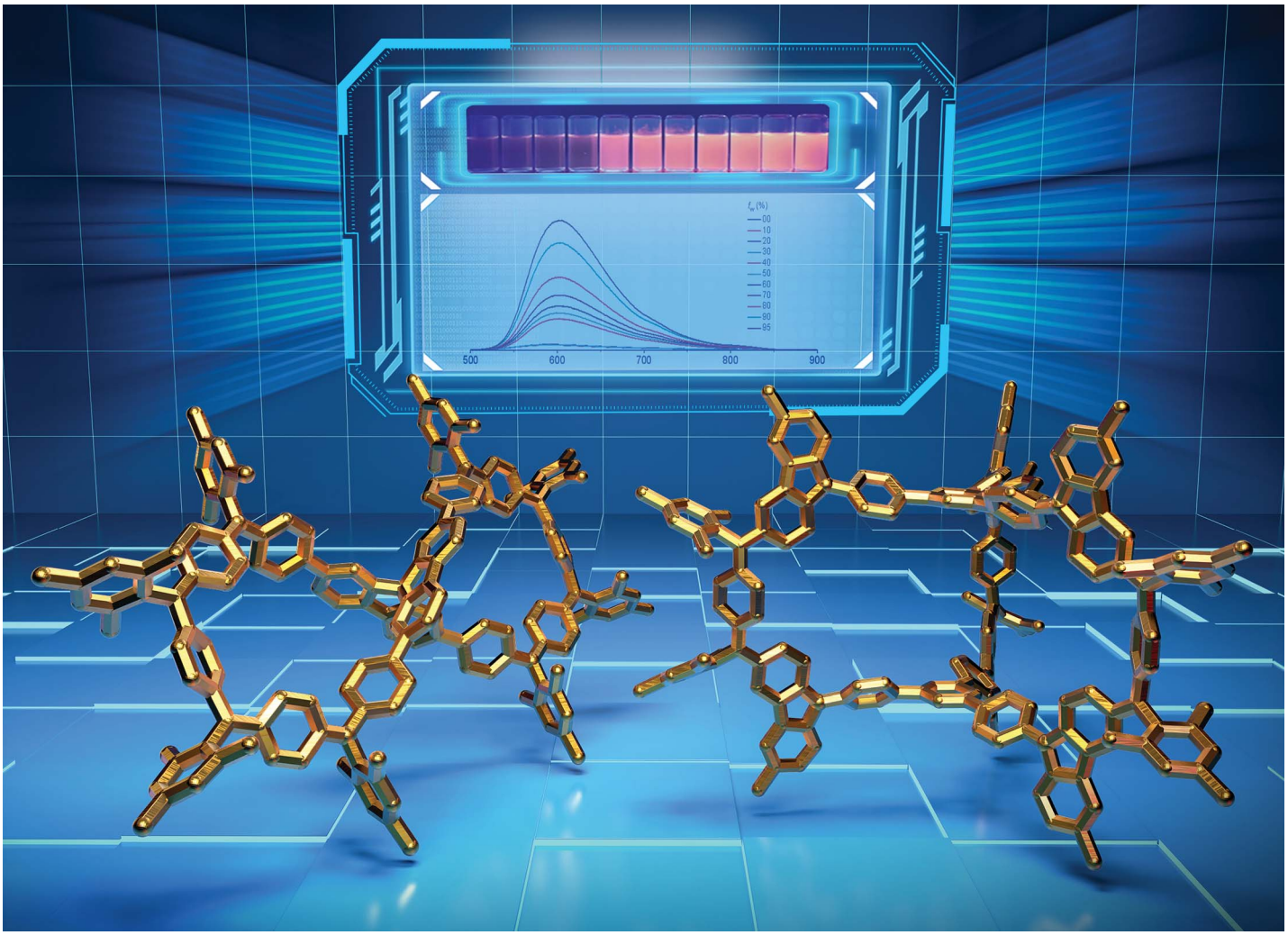

Showcasing research from Professor Prof. Shaoqiang Dong and Prof. Chunyan Chi, Institute of Molecular Aggregation Science, Tianjin University, Tianjin, China and Department of Chemistry, National University of Singapore, Singapore.

Facile synthesis and characterization of aza-bridged all-benzenoid quinoidal figure-eight and cage molecules

Synthesis of conjugated compounds with unusual shape-persistent structures remains a challenge. This paper reported the synthesis of fully π-conjugated figure-eight and cage molecules *via* thermodynamically reversible intermolecular Friedel-Crafts alkylation. These molecules could be oxidized to their cationic species, and showed space-confined intramolecular dynamics and AIE behaviours. The synthetic strategy provides an efficient approach to synthesize potential conjugated 2D or 3D architectures with different topologies and novel optoelectronic properties.

As featured in:

See Shaoqiang Dong, Chunyan Chi *et al.*, *Chem. Sci.*, 2024, **15**, 9087.

ROYAL SOCIETY OF CHEMISTRY

rsc.li/chemical-science

Registered charity number: 207890

Chemical Science

ROYAL SOCIETY OF CHEMISTRY

EDGE ARTICLE

View Article Online
View Journal | View Issue

Cite this: *Chem. Sci.*, 2024, **15**, 9087

All publication charges for this article have been paid for by the Royal Society of Chemistry

Received 29th May 2023
Accepted 27th April 2024

DOI: 10.1039/d3sc02707d

rsc.li/chemical-science

Facile synthesis and characterization of aza-bridged all-benzenoid quinoidal figure-eight and cage molecules†

Shaoqiang Dong, *[ab] Yi Han,[b] Zekun Tong,[a] Jinfeng Wang,[a] Yishan Zhang,[a] Aisen Li,[a] Tullimilli Y. Gopalakrishna,[b] Hongkun Tian[c] and Chunyan Chi *[b]

Synthesis of conjugated compounds with unusual shape-persistent structures remains a challenge. Herein, utilizing thermodynamically reversible intermolecular Friedel–Crafts alkylation, a dynamic covalent chemistry (DCC) reaction, we facilely synthesized a figure-eight shaped macrocycle **FEM** and cage molecules **CATPA**/**CACz**. X-ray crystallographic analysis confirmed the chemical geometries of tetracation $FEM^{4+}(PF_6^-)_4$ and hexacation $CACz^{6+}(SbF_6^-)_6$. **FEM** and **CATPA** displayed higher photoluminescence quantum yield in solid states compared to that in solution, whereas **CACz** gave the reverse result. DFT calculations showed that fluorescence-related frontier molecular orbital profiles are mainly localized on their arms consisting of a *p*-quinodimethane (*p*-QDM) unit and two benzene rings of triphenylamine or carbazole. Owing to their space-confined structures, variable-temperature ^{1}H NMR measurements showed that **FEM**, **CATPA** and FEM^{4+} have intramolecular restricted motion of phenyl rings on their chromophore arms. Accordingly, **FEM** and **CATPA** with flexible triphenylamine subunits displayed aggregation-induced emission behavior (AIE), whereas **CACz** with a rigid carbazole subunits structure showed no AIE behavior.

Introduction

Conjugated nanostructures such as fullerenes, carbon nanotubes and graphene have had revolutionary influence in the areas of chemistry, physics and materials.[1] Recently, novel unusual all-benzenoid shape-persistent structures have attracted scientists' attention, such as carbon nanohoops,[2] nanobelts,[3] extended helicenes,[4] figure-eight[4c–e,5] and bow-knot molecules,[6] molecular cages,[7] catenane and trefoil knots,[8] and open-shell nanographenes.[9] Conversely, methine- or heteroatom-bridged all-benzenoid conjugated nanostructures have been developed, which represent another class of unusual conjugated structures.[10] Study of these materials could elaborate basic chemical concepts such as global aromaticity[10f,g] and bond tautomerization[10f] owing to their alternative quinoidal and aromatic structures. Besides, these novel shape-persistent structures are also endowed with novel physical properties, such as supramolecular behavior owing to their specified cavity[10h,i] or interesting photophysical and optoelectronic properties resulting from the introduction of heteroatoms.[10d,e]

The synthesis of conjugated shape-persistent structures has always been challenging. Kinetically controlled C–C bond reactions for the synthesis of conjugated nanostrucutres usually need expensive metal catalysts or tedious synthetic steps.[2–10]

Dynamic covalent chemistry (DCC) refers to chemical reactions performed reversibly under equilibrium-controlled conditions with self-rectifying character.[11] Friedel–Crafts alkylation is a thermodynamically controlled DCC reaction[12] that has been utilized for the synthesis of macrocyclic compounds. The DCC method also has potential for application in the design and synthesis of more complex and challenging unusual shape-persistent structures. Herein, we report an efficient approach to synthesize figure-eight (**FEM**) and cage (**CATPA** and **CACz**) molecules *via* a metal-free Friedel–Crafts alkylation as the key step (Fig. 1). The **FEM** molecule contains a space-confined pentagon-like geometry on each half. Three-armed **CATPA** shows a flexible conjugated structure, whereas **CACz** exhibits a more rigid structure. Their photophysical properties, redox properties, and molecular dynamics in neutral and cationic states were investigated. Furthermore, these structure-confined molecules provided us good templates to investigate their aggregation-induced emission (AIE) behaviour.

[a]*Institute of Molecular Aggregation Science, Department of Chemistry, Tianjin University, Tianjin 300072, China. E-mail: shqdong@tju.edu.cn*

[b]*Department of Chemistry, National University of Singapore, 3 Science Drive 3, 117543, Singapore. E-mail: chmcc@nus.edu.sg*

[c]*State Key Laboratory of Polymer Physics and Chemistry, Changchun Institute of Applied Chemistry, Chinese Academy of Sciences, Changchun, 130022, China*

† Electronic supplementary information (ESI) available. CCDC 1991177 and 2177038. For ESI and crystallographic data in CIF or other electronic format see DOI: https://doi.org/10.1039/d3sc02707d

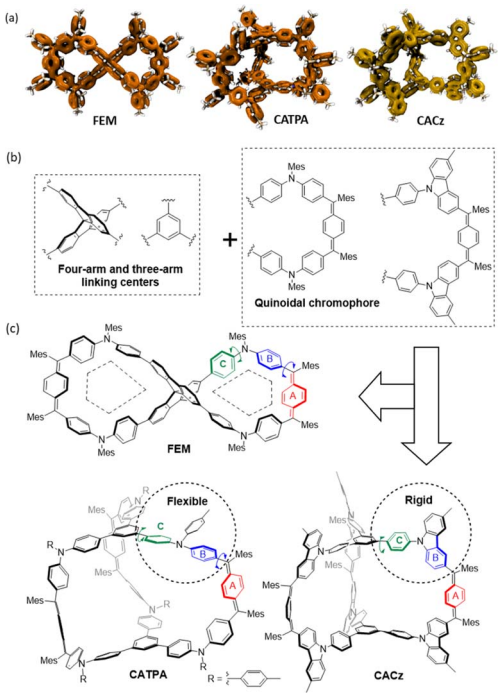

Fig. 1 (a) Localized orbital locator (LOL)-π isosurface maps, (b) building blocks and (c) chemical structures of figure-eight shape (**FEM**) and cage (**CATPA** and **CACz**) molecules.

Results and discussion

Synthesis

All compounds were synthesized by intermolecular Friedel–Crafts alkylation followed by oxidative dehydrogenation reaction (Scheme 1). The intermediate **3** was first prepared *via* a four-fold Suzuki coupling reaction between **1** and **2** in 83% yield. Then, $BF_3 \cdot Et_2O$ mediated the two-fold intermolecular Friedel–Crafts alkylation between **3** and diol **4** in a dilute dichloromethane (DCM) solution to give the figure-eight macrocycle precursor **5**. It was subsequently purified by flash column chromatography and further separated by preparative GPC, yielding 31%. **FEM** was obtained in 54% yield by oxidative dehydrogenation of **5** with 2.2 equivalents of 2,3-dichloro-5,6-dicyano-1,4-benzoquinone (DDQ). Similarly, to synthesize cage compounds **CATPA** and **CACz**, intermediates **9**/**10** were synthesized by three-fold Suzuki coupling reaction between 1,3,5-benzenetriboronic acid tris(pinacol) ester **6** and **7**/**8** in yields of 73%/63%. Subsequent intermolecular Friedel–Crafts cyclization between **9** and diol **4** afforded **11** in 23% yield, and further oxidative dehydrogenation of **11** afforded the target compound **CATPA** in 46% yield. However, intermolecular Friedel–Crafts cyclization between **10** and diol **4** afforded **12** with a yield of around 5%. The relatively low yield of **12** could probably be ascribed to the low reactivity of **10** towards electrophilic cations. Further oxidative dehydrogenation of **12** gave an insoluble yellow solid, and **CACz** could be obtained by recrystallization from toluene with 20% yield. Limited by its poor solubility in common deuterated solvents, ^{1}H NMR measurement of **CACz** did not show any peaks even in hot toluene-d_8; however, the structure of $\mathbf{CACz^{6+}(SbF_6^-)_6}$ could be identified by its ^{1}H NMR spectra (Fig. S47 in ESI†) and X-ray crystallographic analysis. The structures of **FEM** and **CATPA** were identified by ^{1}H and ^{13}C NMR measurements in C_6D_6 (Fig. S30, S31, and S39 in ESI†), and all the protons were assigned by 2D ROESY NMR spectra (Fig. S48 and S51 in ESI†). It is worth noting that **FEM** is racemic with two enantiomers (*P* and *M*), which give identical NMR spectra. However, they could not be resolved after some attempts.

Photophysical properties

UV-vis absorption spectra for **FEM**, **CATPA** and **CACz** were recorded in THF solution (Fig. 2 and Table 1). **FEM**, **CATPA** and **CACz** all show two intense absorption bands centered at 384/

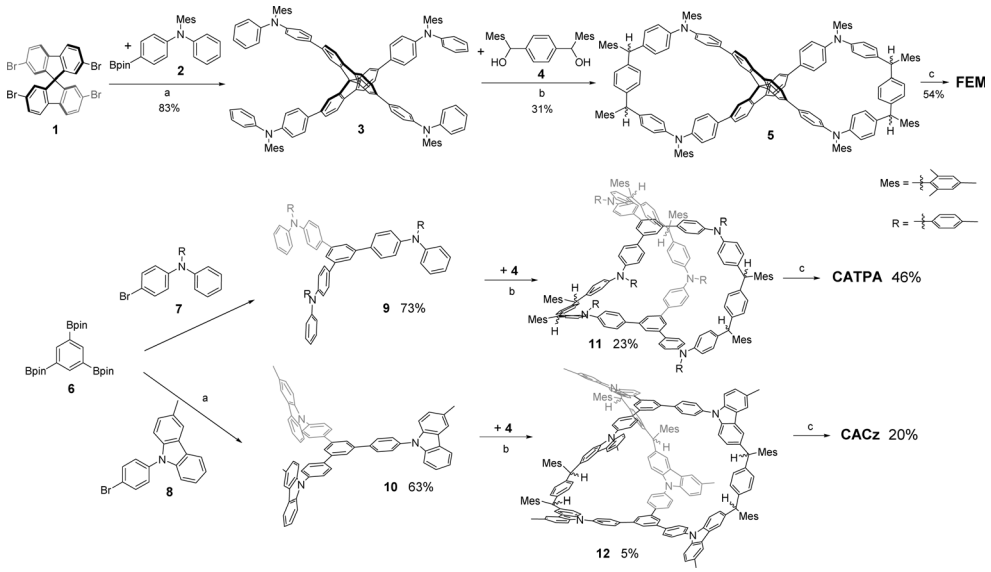

Scheme 1 Synthetic routes for **FEM**, **CATPA** and **CACz**. (a) $Pd(PPh_3)_4$, Na_2CO_3, ethanol, and H_2O. (b) $BF_3 \cdot Et_2O$ and DCM. (c) DDQ, toluene, and acetonitrile. DCM = dichloromethane; DDQ = 2,3-dichloro-5,6-dicyano-1,4-benzoquinone; and Mes: mesityl.

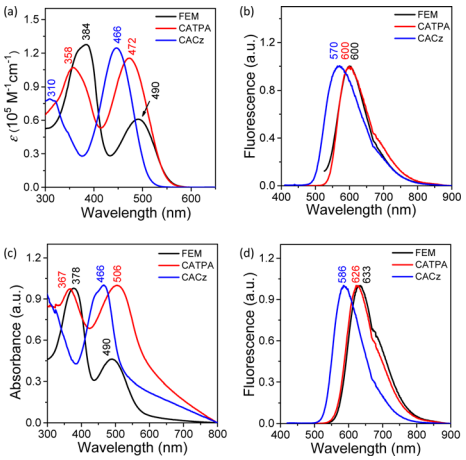

Fig. 2 (a) UV-vis absorption spectra and (b) fluorescence spectra for **FEM**, **CATPA** and **CACz** in THF solution with an excitation wavelength (λ_{ex}) at 365, 395 and 400, respectively; (c) UV-vis absorption spectra and (d) fluorescence spectra for **FEM**, **CATPA** and **CACz** in the thin-film state (λ_{ex} = 400 nm for all three compounds).

490 nm, 358/472 nm and 310/466 nm, respectively (Fig. 2a). DFT calculations indicated that the long-wavelength absorption band of **FEM** is correlated to the synergistic contribution of HOMO → LUMO and HOMO−1 → LUMO+1 electronic transitions (Fig. S12a and Table S3 in ESI†). Similarly, the long-wavelength absorption bands of **CATPA** and **CACz** are correlated to the multiple electronic transitions of HOMO−n to LUMO+m (n, m = 0, 1 and 2). (Fig. S12b, c, Tables S4 and S5 in ESI†). Furthermore, these frontier molecular orbitals are mainly localized along the two half-arms of **FEM** or one-third arms of **CATPA** and **CACz** consisting of the p-QDM ring A and two benzene rings B of triphenylamine or carbazole, respectively (Fig. S11 in ESI†). The absorption spectrum of **CACz** exhibits a hypsochromic shift, probably due to a weak donor–acceptor effect between carbazoles and p-QDM units. In the thin-film state, **FEM** and **CACz** show similar absorption bands and wavelength of absorption maxima to those in solution (Fig. 2a and c), indicating that there is no obvious intermolecular electronic coupling between neighbouring molecules. The wavelength of the absorption maximum of **CATPA** in the thin-film state exhibits a 34 nm red shift, indicating possible intermolecular electronic coupling between adjacent molecules.

The fluorescence spectra of **FEM**, **CATPA** and **CACz** in THF solution are shown in Fig. 2b. **FEM** exhibits one emission peak at 600 nm with a photoluminescence quantum yield (PLQY) of 1.0%. DFT calculations indicated that this emission band is mainly correlated to a synergistic contribution of LUMO+1 → HOMO and LUMO → HOMO−1 radiative transitions (Fig. S12a and Table S6 in ESI†). **CATPA** and **CACz** show one emission peak at 600 and 570 nm with PLQY of 1.2% and 7.4%, respectively. The radiative transitions of **CATPA** and **CACz** are contributed by the multiple electronic transitions of LUMO+m to HOMO−n (n, m = 0, 1 and 2) (Fig. S12b, c, Tables S7 and S8 in ESI†). The Stokes shifts of **FEM**, **CATPA** and **CACz** in THF solution are 110 nm, 128 nm and 104 nm, respectively, indicating the flexible structure of **CATPA**. Furthermore, the fluorescence-related frontier molecular orbital profiles of three compounds are also localized along the arm consisting of rings A and B (Fig. S11 in ESI†). Therefore, the intramolecular dynamic motions of these moieties would have a significant influence on their fluorescence properties.

The fluorescence spectra of **FEM**, **CATPA** and **CACz** in the solid state exhibit a red-shifted emission band with maxima at 633, 626 and 586 nm, respectively (Fig. 2d). In the solid state, **FEM** and **CATPA** show 6- and 4-fold enhanced PLQYs of 6.2% and 4.8%, respectively. Conversely, **CACz** exhibits a decreased PLQY of 4.8% in the solid state. Fluorescence dynamics indicated that, from solution to solid, the enhanced PLQYs of **FEM** and **CATPA** could be explained by about 7-and 4-times increased radiative rate constants, k_r, from 5.8×10^6 s^{-1} and 7.5×10^6 s^{-1} to 4.0×10^7 s^{-1} and 3.4×10^7 s^{-1}, respectively. Meanwhile, non-radiative rate constants, k_{nr}, of **FEM** and **CATPA** only show a slight increase (Table 1), whereas the k_r of **CACz** (1.2×10^8 s^{-1}) in solution is 16 to 20 times higher than those of **FEM** and **CATPA**. From solution to solid state, the k_r of **CACz** decreases by about 6-fold to 2.0×10^7 s^{-1}, and the k_{nr} of **CACz** also decreases from 1.5×10^9 s^{-1} to 4.1×10^8 s^{-1}.

These phenomena could be ascribed to the following: (i) in the solution, the vibration of quinoidal ring A and free rotation of the

Table 1 Photophysical data of **FEM**, **CATPA** and **CACz**

	Solution							Film					
	λ_{abs} [a] (nm)	ε_{max} [b] (10^5 M^{-1} cm^{-1})	λ_{em} [c] (nm)	Φ_F [d] (%)	τ [e] (ns)	k_r [f] (s^{-1})	k_{nr} [g] (s^{-1})	λ_{abs} (nm)	λ_{em} (nm)	Φ_F (%)	τ (ns)	k_r (s^{-1})	k_{nr} (s^{-1})
FEM	384, 490	0.61	600	1.0	1.73	5.8×10^6	5.7×10^8	378, 490	633	6.2	1.54	4.0×10^7	6.1×10^8
CATPA	358, 472	1.15	600	1.2	1.60	7.5×10^6	6.2×10^8	367, 506	626	4.8	1.40	3.4×10^7	6.8×10^8
CACz	310, 466	1.24	570	7.4	0.63	1.2×10^8	1.5×10^9	466	586	4.8	2.35	2.0×10^7	4.1×10^8

[a] λ_{abs}: absorption maximum wavelength. [b] ε_{max}: molar extinction coefficient (M^{-1} cm^{-1}) at the wavelength of the absorption maximum in the low-energy absorption band. [c] λ_{em}: emission maximum wavelength. [d] Φ: photoluminescence quantum yield. [e] τ: fluorescence lifetimes were measured with time-correlated single-photon counting operation mod. [f] k_r: radiative rate constants were calculated with $k_r = \Phi_F/\tau$. [g] k_{nr}: nonradiative rate constants were calculated with $k_{nr} = (1 - \Phi_F)/\tau$.

phenyl ring B (Fig. 1) in **FEM** and **CATPA** would release some energy from their excited states and consequently result in low PLQYs; (ii) in the solid state, the motions of ring A and ring B in **FEM** and **CATPA** are restricted, causing their increased PLQYs; and (iii) due to the rigid chromophores of **CACz**, more energy of the excited states could be released in a radiative way, consequently causing its moderate PLQYs in solution and film state.

Electrochemical properties and chemical oxidation

FEM and **CATPA** display only one reversible oxidation wave with half-wave potential, $E_{ox}^{1/2}$, at −0.23 V and −0.14 V (*vs.* Fc^+/Fc couple) and irreversible reduction wave with half-wave potential, $E_{red}^{1/2}$, at −2.36 V, −2.33 V, respectively (Fig. S6a, b and Table S2 in ESI†). **CACz** in 1,2-dichlorobenzene at 80 °C displays only a reversible oxidation wave with $E_{ox}^{1/2}$ at 0.00 V, and no reduction wave could be observed (Fig. S6c in ESI†).

The dication $\mathbf{FEM^{2(\cdot+)}(SbF_6^-)_2}$ and triradical trication $\mathbf{CATPA^{3(\cdot+)}(SbF_6^-)_3}$/$\mathbf{CACz^{3(\cdot+)}(SbF_6^-)_3}$ were generated in dry DCM by adding two and three equivalents of silver hexafluoroantimonate ($AgSbF_6$) to their neutral compounds, and they showed intense ESR signals in solution with *g* values of 2.0027 and 2.0028/2.0030 (Fig. S3†), respectively. Additionally, $\mathbf{FEM^{2(\cdot+)}(SbF_6^-)_2}$, $\mathbf{CATPA^{3(\cdot+)}(SbF_6^-)_3}$ and $\mathbf{CACz^{3(\cdot+)}(SbF_6^-)_3}$ exhibit similar broad long-wavelength absorption bands with λ_{max} at 1000/1183, 990/1169 and 919/1072 nm, respectively (Fig. 3, S7a, S8a and S9a†). DFT calculations revealed that $\mathbf{FEM^{2(\cdot+)}(SbF_6^-)_2}$ and $\mathbf{CATPA^{3(\cdot+)}(SbF_6^-)_3}$/$\mathbf{CACz^{3(\cdot+)}(SbF_6^-)_3}$ contain two or three separated mono radicals with spin densities located at each quinoidal arm, respectively (Fig. S10†). The tetracation $\mathbf{FEM^{4+}(SbF_6^-)_4}$ and hexacations $\mathbf{CATPA^{6+}(SbF_6^-)_6}$/$\mathbf{CACz^{6+}(SbF_6^-)_6}$ were generated by chemical oxidation with four and six equivalents of $AgSbF_6$, respectively. These tetra- and hexacations are all ESR silent and show clear ^{1}H NMR spectra at 298 K (Fig. S32, S40 and S47†), indicating their closed-shell character. The protons of $\mathbf{FEM^{4+}(SbF_6^-)_4}$ and $\mathbf{CATPA^{6+}(SbF_6^-)_6}$ are well assigned by 2D ROESY NMR (Fig. S49, S50 and S52†). UV-Vis-NIR absorption spectra for $\mathbf{FEM^{4+}(SbF_6^-)_4}$ display two major absorption bands with λ_{max} at 344/511 nm. UV-Vis-NIR absorption spectra for $\mathbf{CATPA^{6+}(SbF_6^-)_6}$ and $\mathbf{CACz^{6+}(SbF_6^-)_6}$ show a main peak at 505 and 419 nm with a shoulder band at 600 and 500 nm extended to the near-infrared region, respectively.

Intramolecular dynamic motions

The space-confined structures of the figure-eight and cage molecules provoked us to investigate their molecular dynamics. Variable-temperature (VT) ^{1}H NMR spectra for **FEM** in toluene-

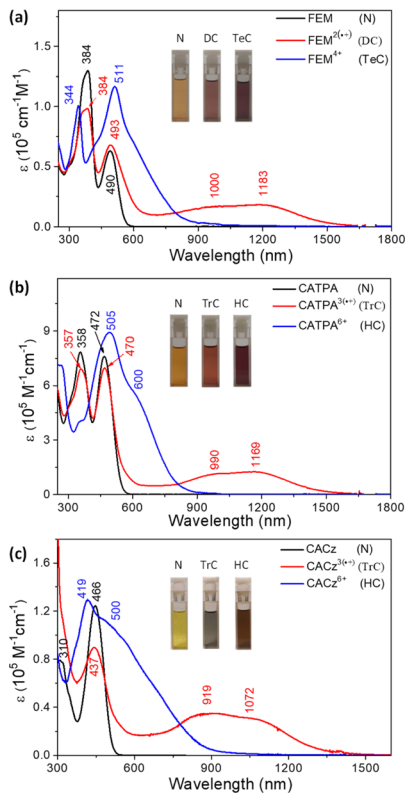

Fig. 3 (a) UV-Vis-NIR absorption spectra for **FEM**, $\mathbf{FEM^{2(\cdot+)}}$ and $\mathbf{FEM^{4+}}$ generated by chemical titration with $AgSbF_6$. (b) UV-vis-NIR absorption spectra for **CATPA**, $\mathbf{CATPA^{3(\cdot+)}}$ and $\mathbf{CATPA^{6+}}$. (c) UV-vis-NIR absorption spectra for **CACz**, $\mathbf{CACz^{3(\cdot+)}}$ and $\mathbf{CACz^{6+}}$ (insets are their photographs in DCM). N: neutral; DC: dication; TrC: trication; TeC: tetracation; HC: hexacation.

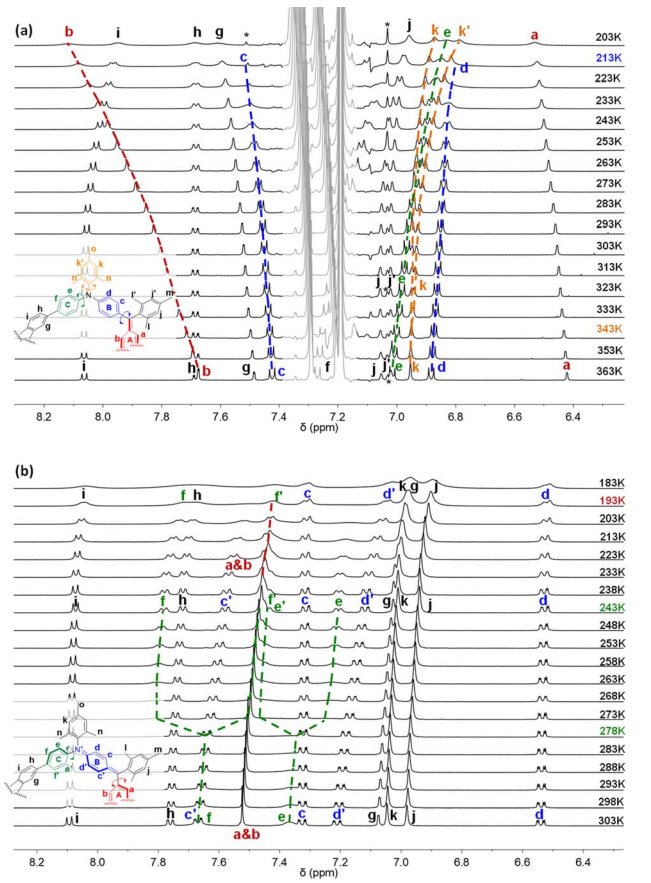

Fig. 4 VT ^{1}H NMR spectra (aromatic region) for (a) **FEM** and (b) $\mathbf{FEM^{4+}(SbF_6^-)_4}$ in toluene-d_8. Dashed lines showed the changes of protons on the A (red), B (blue) and C (green) rings with temperature. * indicates the residue from toluene-d_8. One quarter of the chemical structure of **FEM** and $\mathbf{FEM^{4+}}$ is shown.

d_8 (Fig. 4a) show that, upon cooling, protons *k* of mesityl groups on N atoms split into two singlet peaks (k and k′) with coalescence temperature (T_c) at 343 K, indicating the slowed-down rotation of the mesityl groups. From 363 K to 203 K, protons c and d on ring B also gradually become broad and fully coalesce at 213 K. Limited by the solubility of **FEM** in toluene, all the other peaks in the aromatic region become broad upon further cooling. Similar to other macrocyclic skeletons,[13] this phenomenon can be explained by the flipping ceasing process of B rings at low temperature, which caused the low-field movement of proton b with a $\Delta\delta$ of 0.44 ppm. DFT calculated the strain energy of **FEM** *via* hypothetical homodesmotic reactions[14] (Scheme S1 in ESI†) to be −9.0 kcal mol^{-1}, which is much smaller than those of all-benzenoid aromatic nanohoops and nanobelts[5a,b,15] for the introduction of bridged atoms.

VT ^{1}H NMR spectra for **FEM**$^{4+}$(**SbF**$_6^-$)$_4$ in CD_2Cl_2 are shown in Fig. 4b. At 298 K, protons c and d on the B rings split into two sets of signals for the formation of localized N$^+$-doped *p*-QDMs, accompanied by the formation of benzenoid A rings with two protons a and b merging into one a & b peak. Upon cooling, the flipping of C rings slows down, and the resonances of protons e and f coalesce at 278 K and finally split into two sets of signals e/e′ and f/f′ at 243 K. Upon further cooling, protons a & b also gradually coalesce at 193 K. The exchange rate constants (*k*) of the protons on the C rings at different temperatures were obtained by line shape analysis (Section 2 in the ESI†), and fitting of the data by the Eyring equation ($\ln(k/T) = -(\Delta H^{\ddagger}/R)\cdot 1/T + \ln(k_B/h) + \Delta S^{\ddagger}/R$) gave thermodynamic parameters $\Delta H^{\ddagger} = 22.1 \pm 0.5$ kcal mol^{-1} and $\Delta S^{\ddagger} = 32.8 \pm 1.7$ cal (mol^{-1} K^{-1}) (Table S1 and Fig. S1 in ESI†). Accordingly, the interconversion energy $\Delta G^{\ddagger}$ of the C rings at 243 K was estimated to be 13.0 ± 0.9 kcal mol^{-1}. This can be explained by its more confined structure induced by two newly formed N$^+$-doped *p*-QDMs and the corresponding Coulomb repulsion between two positively charges. Therefore, DFT calculations gave a larger strain energy of −24.7 kcal mol^{-1} (Scheme S1 in ESI†).

VT ^{1}H NMR spectra for **CATPA** in toluene-d_8 (Fig. S4 in ESI†) show that *p*-tolyl groups on N atoms can freely rotate even upon cooling due to its lower steric hindrance. Protons c and d on ring B gradually become broad, and fully coalesce around 208 K. Proton b also shows low-field movement upon cooling; however, the small $\Delta\delta$ of 0.17 ppm indicates the weak deshielding effect from the B rings. This could originate from its small strain energy of −7.3 kcal mol^{-1} (Scheme S1 in ESI†). In VT ^{1}H NMR spectra for **CATPA**$^{6+}$(**SbF**$_6^-$)$_6$ (Fig. S5†), upon cooling, protons (c, c′, d and d′) on the ring B show slight high-field movement, which could be ascribed to the weak shielding effect of the A and C rings.

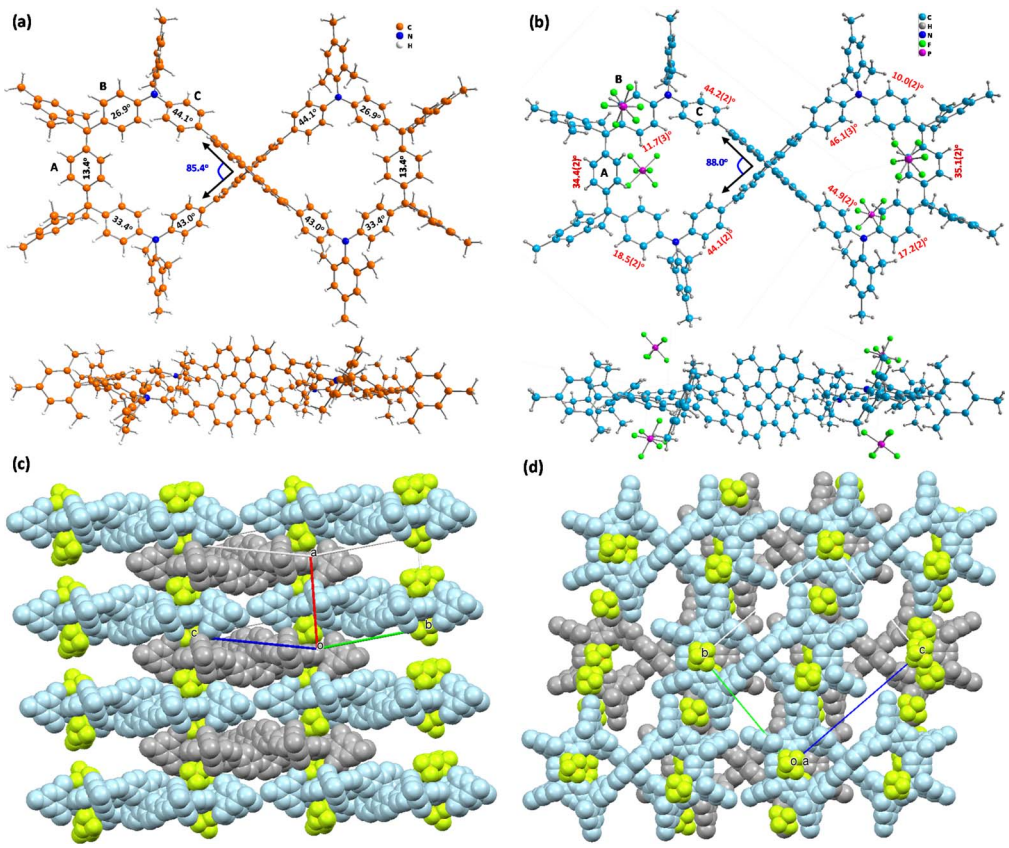

Fig. 5 (a) DFT optimized structure of **FEM** (*M*-enantiomer) and (b) X-ray crystallographic structure of **FEM**$^{4+}$(PF$_6^-$)$_4$ with top and side views (*M*-enantiomer was shown only). (c and d) Packing motifs of **FEM**$^{4+}$(PF$_6^-$)$_4$ were shown in space filling model with side and top view. *P*-Enantiomers are shown in light blue colour, and *M*-enantiomers are shown in light grey colour; counter anions are shown in light green colour. Solvent molecules are omitted.

Ground-state geometry

The geometry of **FEM** (*M*-enantiomer) was optimized by DFT calculations (Fig. 5a). The dihedral angles of the rings A, B and C with respect to the plane of each half, determined using the sp^3 C atom on spirofluorene (**SBF**) and two meso C atoms, are 13.4°, 26.9°/33.4°, and 44.1°/43.0°, respectively. Obviously, the A rings are less distorted than the B and C rings due to the quinoidal character of the A rings. In each half-cycle, five phenyl rings show alternating up-down conformation, which can help to release the strain energy caused by the steric repulsion.

$\mathbf{FEM^{4+}(PF_6^-)_4}$ was obtained by the chemical oxidation of **FEM** with four equivalents of silver hexafluorophosphate ($AgPF_6$). The ^{1}H NMR spectrum of $\mathbf{FEM^{4+}(PF_6^-)_4}$ (Fig. S34 in ESI†) is almost identical to that of $\mathbf{FEM^{4+}(SbF_6^-)_4}$. Single-crystal $\mathbf{FEM^{4+}(PF_6^-)_4}$ (ref. 16) (Fig. 5b–d) crystalizes in the $P\bar{1}$ group, and the four counter anions $\mathbf{PF_6^-}$ are located well above and below the center of each half-cycle (Fig. 5b). The angle between the two phenyl rings of **SBF** in one half-cycle is 88.0°. Similarly, the phenyl rings in each half also show alternating up-down conformation. In its packing structure (Fig. 5c and d), the *P*-enantiomer (light blue) and *M*-enantiomer (grey) are arranged in a three-dimensional (3D) superstructure. Along the *a* axis (Fig. 5c and S16a in ESI†), *P*-enantiomers and *M*-enantiomers are overlapped alternatingly with their half of the molecules, forming a columnar structure. The top view of the packing along the *bc* plane is shown in Fig. 5d and 16b in the ESI.† This packing structure is stabilized by multiple [C–H···F] (2.294(6)–2.669(6) Å, Fig. S17a and Table S11 in ESI†) and [C···F] (3.048(10)/3.055(13)/3.164(11) Å, Fig. S17b and Table S12 in ESI†) and [C–H···C] (2.713(12)–2.896(12) Å, Fig. S17c and Table S13 in ESI†) interactions, which leads to the formation of a closely packed 3D network. For comparison, dihedral angles (Fig. 5b) of the A, B and C rings of $\mathbf{FEM^{4+}(PF_6^-)_4}$ with respect to the plane of each half determined using the sp^3 C atom on **SBF** and two meso C atoms are 34.4(2)°/35.1(2)°, 11.7(3)°/18.5(2)°/10.0(2)°/17.2(2)°, and 44.2(2)°/44.1(2)°/46.1(3)°/44.9(2)°, respectively. Compared to the neutral structure, the four B rings become less distorted than A rings and C rings due to their quinoidal structures.

Localized orbital locator (LOL) π-electrons analysis was performed based on wavefunction analysis code Multiwfn[17] to investigate the π-conjugated pathway. The LOL-π isosurface maps of **FEM** and $\mathbf{FEM^{4+}}$ with an isovalue of 0.2 (Fig. 1 and S13 in ESI†) reveal that the π-electrons are delocalized along entire molecular backbones except for sp^3 C, indicating a fully conjugated structure. For **FEM** and $\mathbf{FEM^{4+}}$, two twisted figure-

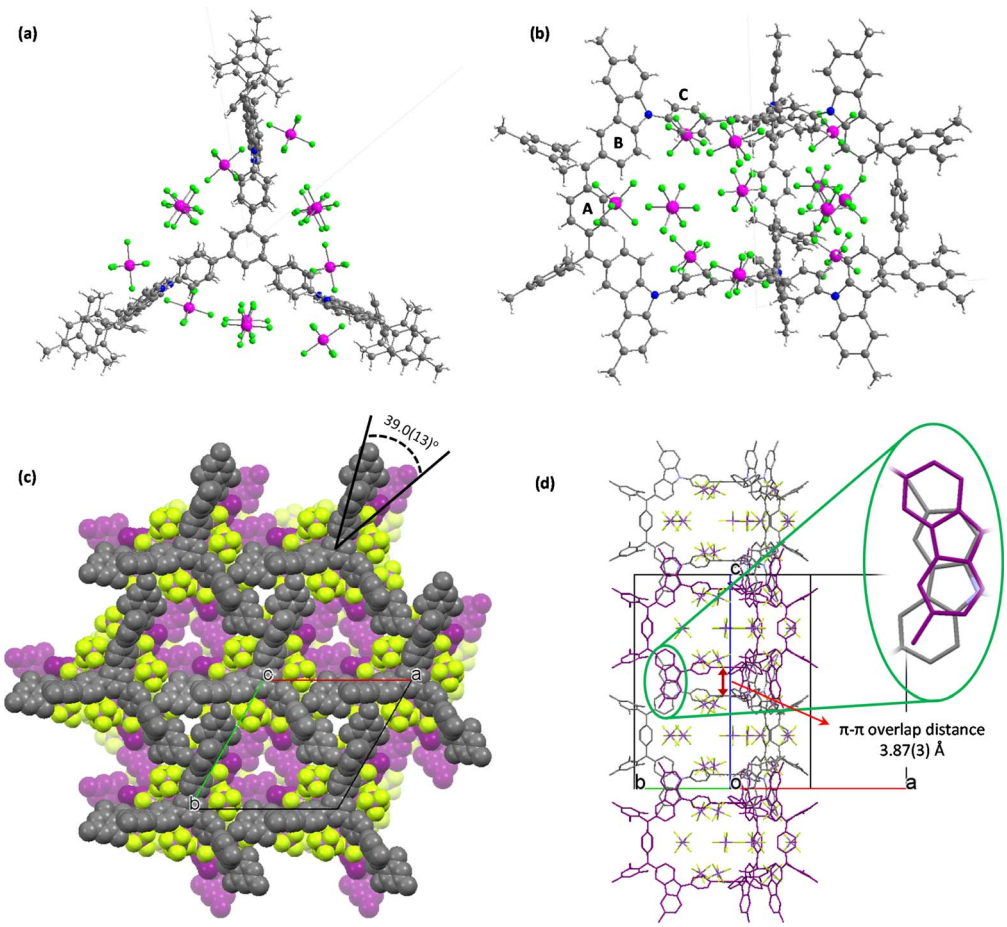

Fig. 6 X-ray crystallographic structure of $\mathbf{CACz^{6+}(SbF_6^-)_6}$ with (a) top view and (b) side view. (c and d) Packing motifs of $\mathbf{CACz^{6+}(SbF_6^-)_6}$ are shown in a space filling model with top and side views. Two layers in alternative colours of grey and purple are shown, and counter anions are shown in light green colour.

eight π-electron pathways catenate together, and each one shows near-planar π-conjugation along two half-cycles at the same side of the molecular surface and radial π-conjugation[2] along the central **SBF** unit (Fig. S13†). In addition, the calculated anisotropy of the induced current density (ACID)[18] plots of **FEM** and **FEM^{4+}** (Fig. S15 in ESI†) show their quinoidal structures and localized aromatic phenyl rings. Similarly, **CATPA**, **CATPA^{6+}**, **CACz** and **CACz^{6+}** are also fully conjugated cages with localized aromatic character (Fig. 1 and S14 in the ESI†).

Single-crystal **CACz^{6+}(SbF$_6^-$)$_6$** (ref. 16) crystalizes in the $P\bar{6}2c$ group, with six **SbF$_6^-$** counter anions located around **CACz6+**, with twelve occupied positions owing to the random distribution of **SbF$_6^-$** (Fig. 6a and b). In its packing structure (Fig. 6c), a hexagonal lattice layer is formed with one **CACz^{6+}(SbF$_6^-$)$_6$** molecule surrounded by six neighbour molecules in one layer. Three **CACz^{6+}(SbF$_6^-$)$_6$** molecules form a triangle structure with one arm going to the concave position of adjacent molecules, which is also stabilized by the [C···F] (3.05(4) Å) interaction of **SbF$_6^-$** and carbons on ring A, multiple [C–H···F] (2.39(2)–2.55(2) Å) interactions of **SbF$_6^-$** and protons on the ring B, mesityl group and central phenyl ring (Fig. S18a and Table S14 in ESI†), [C···C] (3.22(3) Å) and multiple [C–H···C] interactions (2.79(2)–2.852(17) Å) between the ring B and neighbouring carbazoles (Fig. S18b and Table S15 in ESI†). Along the *c* axis, **CACz^{6+}(SbF$_6^-$)$_6$** molecules arrange themselves in columnar fashion, with two neighbouring molecules featuring a rotation angle of 39.0(13)° and π–π overlap distance of 3.87(3) Å between the two central phenyl rings (Fig. 6d). Additionally, the rotation of two stacking molecules leads to three sets of carbazole moieties exhibiting π–π overlap distances of around 3.39(5) Å–3.57(2) Å, resulting in the formation of an interpenetrating column structure.

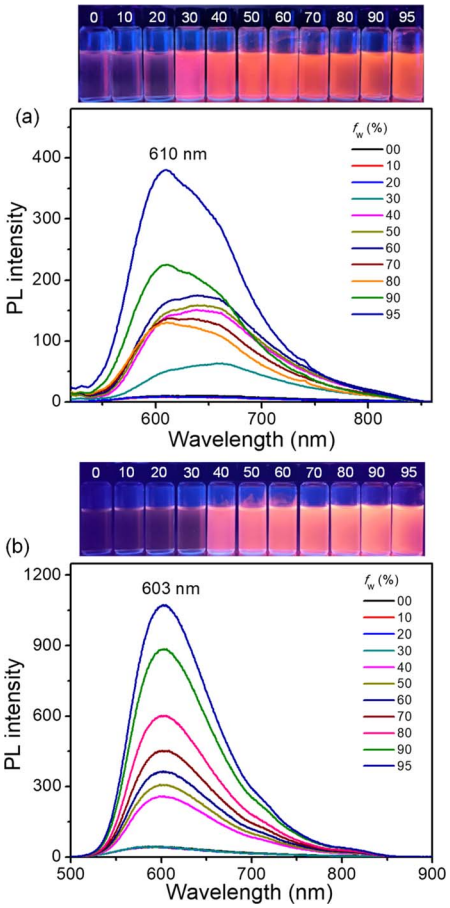

Fig. 7 Photoluminescence (PL) spectra (1.5×10^{-5} m, $\lambda_{ex} = 400$ nm) for (a) FEM and (b) CATPA in THF/H_2O mixed solvents with different H_2O fractions (f_w) (insets are PL photographs of FEM and CATPA with different water fractions under 365 nm UV irradiation).

Aggregation-induced emission

Considering the increased PLQYs of **FEM**/**CATPA** and decreased PLQY of **CACz** from solution to the solid state, photoluminescence measurements were conducted in THF/H_2O mixed solvents with different water fractions to examine their potential AIE behavior.[19] As shown in Fig. 7, by increasing the water fraction (f_w) of the mixed solvents, the emission intensity of **FEM** and **CATPA** increased, accompanied by a slight blue shift of the wavelength of the emission maximum. Eventually, the ratio of I/I_0 (I_0 and I represent the emission intensity at the maximum emission wavelength when f_w is 0% and corresponding water fractions, respectively) reached maximum saturation values of 38 and 23 for **FEM** and **CATPA**, respectively. Therefore, both compounds showed the typical phenomena of AIE fluorogens (AIEgens), whereas **CACz** did not show AIE behavior (Fig. S21†).

Molecular fluorescence dynamics indicate that the k_{nr}/k_r ratios of FEM and CATPA decreased from 98 and 83 in solution to 15 and 20 in the solid state, respectively. Therefore, the weak emissions of FEM and CATPA in pure THF solution can be ascribed to the non-radiative energy consumption. Since their HOMO−*n* and LUMO+*m* (*n*, *m* = 0, 1 and 2) coefficients are mainly localized on quinoidal arms, their emission band can be significantly affected by the intramolecular motions of the A and B rings. The energy of the excited state would probably be released by free intramolecular rotations of the B rings or vibrations of *p*-QDM A units in the solution. With the increase of the water fraction, the formation of aggregates would limit the free motions of these rings. Therefore, the AIE phenomena of FEM and CATPA can be explained by the restriction of the intramolecular motion mechanism observed in other AIEgen systems.[19] Our findings here provide a new class of quinoidal AIEgens with orange light emission.

Conclusions

Spirofluorene-bridged figure-eight shaped macrocycle **FEM** and 1,3,5-tribenzene-bridged cage molecules **CATPA**/**CACz** were facilely synthesized by intermolecular Friedel–Crafts alkylation followed by oxidative dehydrogenation. Four-electron and six-electron chemical oxidation produced their respective tetracation **FEM^{4+}** and hexacation **CATPA6+**/**CACz6+**. Single-crystal analysis of **FEM^{4+}** revealed its figure-eight geometry with a closely packed 3D network. Single-crystal analysis of **CACz^{6+}(SbF$_6^-$)$_6$** revealed its cage geometry and tightly packed

interpenetrating hexagonal lattice structure. VT-NMR measurements of **FEM/CATPA** and **FEM**$^{4+}$ clearly revealed their unique temperature-dependent intramolecular dynamic motions, which originated from their space-confined chemical structures. This dynamic process has a significant impact on their emission properties from solution to aggregate or solid state, and AIE behavior was observed for **FEM/CATPA**, whereas **CACz** with a rigid conjugated structure showed no AIE behavior. The macrocyclic and cage-like structures reported in this work are also a new class of quinoidal AIEgens and are a good addition to the AIE family. Our dynamic covalent chemistry method provides an efficient approach that could be used to synthesize conjugated 2D or 3D architectures with different topologies and novel optoelectronic properties in the future.

Data availability

Experimental synthetic procedures, characterization data and theoretical calculation results are available in the ESI.†

Author contributions

S. Dong performed the synthetic and characterization work, J. Wang, A. Li, and Y. Zhang carried out spectroscopic measurements and data analysis, Y. Han and T. Y. Gopalakrishna conducted and analysed the computational results, H. Tian conducted the X-ray crystallographic analysis, S. Dong and C. Chi concepted the work and wrote the paper.

Conflicts of interest

There are no conflicts to declare.

Acknowledgements

The research at National University of Singapore was supported by MOE Tier 1 grant (A-8000992-00-00), MOE Tier 2 grants (MOE-MOET2EP10120-0006 and MOET2EP10222-0008) and A*STAR AME MTC YIRG project (M21K3c0128). The research in China was supported by Natural Science Foundation of China (22175128) and starting grants of Tianjin University.

References

1 (*a*) H. W. Kroto, J. R. Heath, S. C. O'Brien, R. F. Curl and R. E. Smalley, *Nature*, 1985, **318**, 162; (*b*) S. Iijima, *Nature*, 1991, **354**, 56; (*c*) K. S. Novoselov, A. K. Geim, S. V. Morozov, D. Jiang, Y. Zhang, S. V. Dubonos, I. V. Grigorieva and A. A. Firsov, *Science*, 2004, **306**, 666.

2 (*a*) S. Yamago, E. Kayahara and T. Iwamoto, *Chem. Rec.*, 2014, **14**, 84; (*b*) M. R. Golder and R. Jasti, *Acc. Chem. Res.*, 2015, **48**, 557; (*c*) Y. Segawa, A. Yagi, K. Matsui and K. Itami, *Angew. Chem., Int. Ed.*, 2016, **55**, 5136.

3 (*a*) G. Povie, Y. Segawa, T. Nishihara, Y. Miyauchi and K. Itami, *Science*, 2017, **356**, 172; (*b*) Z. Sun, K. Ikemoto, T. M. Fukunaga, T. Koretsune, R. Arita, S. Sato and H. Isobe, *Science*, 2019, **363**, 151; (*c*) K. Y. Cheung, S. Gui, C. Deng, H. Liang, Z. Xia, Z. Liu, L. Chi and Q. Miao, *Chem*, 2019, **5**, 838; (*d*) S. Nishigaki, Y. Shibata, A. Nakajima, H. Okajima, Y. Masumoto, T. Osawa, A. Muranaka, H. Sugiyama, A. Horikawa, H. Uekusa, H. Koshino, M. Uchiyama, A. Sakamoto and K. Tanaka, *J. Am. Chem. Soc.*, 2019, **141**, 14955; (*e*) T. Shi, Q. Guo, S. Tong and M. Wang, *J. Am. Chem. Soc.*, 2020, **142**, 4576; (*f*) H. Chen, S. Gui, Y. Zhang, Z. Liu and Q. Miao, *CCS Chem.*, 2020, **3**, 613; (*g*) Y. Han, S. Dong, J. Shao, W. Fan and C. Chi, *Angew. Chem., Int. Ed.*, 2021, **133**, 2690; (*h*) K. Y. Cheung, K. Watanabe, Y. Segawa and K. Itami, *Nat. Chem.*, 2021, **13**, 255; (*i*) Z. Xia, S. H. Pun, H. Chen and Q. Miao, *Angew. Chem., Int. Ed.*, 2021, **60**, 10311; (*j*) Y. Segawa, T. Watanabe, K. Yamanoue, M. Kuwayama, K. Watanabe, J. Pirillo, Y. Hijikata and K. Itami, *Nat. Synth.*, 2022, **1**, 535; (*k*) H. Chen, Z. Xia and Q. Miao, *Chem. Sci.*, 2022, **13**, 2280.

4 (*a*) A. Robert, P. Dechambenoit, E. A. Hillard, H. Bock and F. Durola, *Chem. Commun.*, 2017, **53**, 11540; (*b*) X. Jiang, J. D. Laffoon, D. Chen, S. Pérez-Estrada, A. S. Danis, J. Rodríguez-López, M. A. Garcia-Garibay, J. Zhu and J. S. Moore, *J. Am. Chem. Soc.*, 2020, **142**, 6493; (*c*) G. R. Kiel, K. L. Bay, A. E. Samkian, N. J. Schuster, J. B. Lin, R. C. Handford, C. Nuckolls, K. N. Houk and T. D. Tilley, *J. Am. Chem. Soc.*, 2020, **142**, 11084; (*d*) W. Fan, T. Matsuno, Y. Han, X. Wang, Q. Zhou, H. Isobe and J. Wu, *J. Am. Chem. Soc.*, 2021, **143**, 15924; (*e*) M. Krzeszewski, H. Ito and K. Itami, *J. Am. Chem. Soc.*, 2022, **144**, 862.

5 (*a*) K. Senthilkumar, M. Kondratowicz, T. Lis, P. J. Chmielewski, J. Cybińska, J. L. Zafra, J. Casado, T. Vives, J. Crassous, L. Favereau and M. Stępień, *J. Am. Chem. Soc.*, 2019, **141**, 7421; (*b*) T. A. Schaub, E. A. Prantl, J. Kohn, M. Bursch, C. R. Marshall, E. J. Leonhardt, T. C. Lovell, L. N. Zakharov, C. K. Brozek, S. R. Waldvogel, S. Grimme and R. Jasti, *J. Am. Chem. Soc.*, 2020, **142**, 8763; (*c*) L. Zhan, C. Dai, G. Zhang, J. Zhu, S. Zhang, H. Wang, Y. Zeng, C. Tung, Li. Wu and H. Cong, *Angew. Chem., Int. Ed.*, 2022, **61**, e202113334.

6 (*a*) Z. Huang, C. Chen, X. Yang, X. Fan, W. Zhou, C. Tung, L. Wu and H. Cong, *J. Am. Chem. Soc.*, 2016, **138**, 11144; (*b*) W. Xu, X. Yang, X. Fan, X. Wang, C. Tung, L. Wu and H. Cong, *Angew. Chem., Int. Ed.*, 2019, **58**, 3943; (*c*) L. Wang, N. Hayase, H. Sugiyama, J. Nogami, H. Uekusa and K. Tanaka, *Angew. Chem., Int. Ed.*, 2022, **59**, 17951.

7 (*a*) E. Kayahara, T. Iwamoto, H. Takaya, T. Suzuki, M. Fujitsuka, T. Majima, N. Yasuda, N. Matsuyama, S. Seki and S. Yamago, *Nat. Commun.*, 2013, **4**, 2694; (*b*) K. Matsui, Y. Segawa and K. Itami, *J. Am. Chem. Soc.*, 2014, **136**, 16452; (*c*) S. Cui, G. Zhuang, D. Lu, Q. Huang, H. Jia, Y. Wang, S. Yang and P. Du, *Angew. Chem., Int. Ed.*, 2018, **130**, 9330; (*d*) M. Mastalerz, *Acc. Chem. Res.*, 2018, **51**, 2411; (*e*) N. Hayase, J. Nogami, Y. Shibata and K. Tanaka, *Angew. Chem., Int. Ed.*, 2019, **58**, 9439; (*f*) J. Zhu, Y. Han, Y. Ni, S. Wu, Q. Zhang, T. Jiao, Z. Li and J. Wu, *J. Am. Chem. Soc.*, 2021, **143**, 14314.

8 (*a*) Y. Fan, D. Chen, Z. Huang, J. Zhu, C. Tung, L. Wu and H. Cong, *Nat. Commun.*, 2018, **9**, 3037; (*b*) Y. Segawa,

M. Kuwayama, Y. Hijikata, M. Fushimi, T. Nishihara, J. Pirillo, J. Shirasaki, N. Kubota and K. Itami, *Science*, 2019, **365**, 272; (*c*) Y. Segawa, D. R. Levine and K. Itami, *Acc. Chem. Res.*, 2019, **52**, 2760; (*d*) B. P. Benke, T. Kirschbaum, J. Graf, J. H. Gross and M. Mastalerz, *Nat. Chem.*, 2023, **15**, 413.

9 (*a*) M. Abe, *Chem. Rev.*, 2013, **113**, 7011; (*b*) Z. Sun, Z. Zeng and J. Wu, *Acc. Chem. Res.*, 2014, **47**, 2582; (*c*) Z. Zeng, X. Shi, C. Chi, J. T. L. Navarrete, J. Casado and J. Wu, *Chem. Soc. Rev.*, 2015, **44**, 6578; (*d*) T. Kubo, *Chem. Lett.*, 2015, **44**, 111; (*e*) T. Y. Gopalakrishna, W. Zeng, X. Lu and J. Wu, *Chem. Commun.*, 2018, **54**, 2186; (*f*) C. Liu, Y. Ni, X. Lu, G. Li and J. Wu, *Acc. Chem. Res.*, 2019, **52**, 2309; (*g*) W. Zeng and J. Wu, *Chem*, 2020, **7**, 358; (*h*) S. Dong and Z. Li, *J. Mater. Chem. C*, 2022, **10**, 2431.

10 (*a*) V. A. Sergeev, V. I. Nedel'kin and O. B. Andrianova, *Vysokomol. Soedin., Ser. B*, 1987, **29**, 357; (*b*) V. A. Sergeev, V. I. Nedel'kin, A. V. Astankov, A. V. Nikiforov, E. M. Alov and Y. A. Moskvichev, *Izv. Akad. Nauk, Ser. Khim.*, 1990, 763; (*c*) D. Takeuchi, I. Asano and K. Osakada, *J. Org. Chem.*, 2006, **71**, 8614; (*d*) A. Ito, Y. Yokoyama, R. Aihara, K. Fukui, S. Eguchi, K. Shizu, T. Sato and K. Tanaka, *Angew. Chem., Int. Ed.*, 2010, **49**, 8205; (*e*) P. Chen, R. A. Lalancette and F. Jäkle, *Angew. Chem., Int. Ed.*, 2012, **51**, 7994; (*f*) Y. Ni, M. E. Sandoval-Salinas, T. Tanaka, H. Phan, T. S. Herng, T. Y. Gopala-krishna, J. Ding, A. Osuka, D. Casanova and J. Wu, *Chem*, 2019, **5**, 108; (*g*) Z. Li, T. Y. Gopalakrishna, Y. Han, Y. Gu, L. Yuan, W. Zeng, D. Casanova and J. Wu, *J. Am. Chem. Soc.*, 2019, **141**, 16266; (*h*) G. Li, T. Matsuno, Y. Han, H. Phan, S. Wu, Q. Jiang, Y. Zou, H. Isobe and J. Wu, *Angew. Chem., Int. Ed.*, 2020, **59**, 9727; (*i*) Y. Ni, F. Gordillo-Gámez, M. P. Alvarez, Z. Nan, Z. Li, S. Wu, Y. Han, J. Casado and J. Wu, *J. Am. Chem. Soc.*, 2020, **142**, 12730.

11 (*a*) S. J. Rowan, S. J. Cantrill, G. R. L. Cousins, J. K. M. Sanders and J. F. Stoddart, *Angew. Chem., Int. Ed.*, 2002, **41**, 898; (*b*) M. E. Belowich and J. F. Stoddart, *Chem. Soc. Rev.*, 2012, **41**, 2003; (*c*) Y. Jin, Q. Wang, P. Taynton and W. Zhang, *Acc. Chem. Res.*, 2014, **47**, 1575.

12 (*a*) Y. Jin, C. Yu, R. J. Denman and W. Zhang, *Chem. Soc. Rev.*, 2013, **42**, 6634; (*b*) M. J. Earle, G. Roberts and K. R. Seddon, *Chem. Commun.*, 1998, 2097; (*c*) M. Holler, N. Allenbach, J. Sonet and J.-F. Nierengarten, *Chem. Commun.*, 2012, **48**, 2576; (*d*) X. Xie, Y. Wei, D. Lin, C. Zhong, L. Xie and W. Huang, *Chin. J. Chem.*, 2020, **38**, 103; (*e*) B. K. Reddy, A. Basavarajappa, M. D. Ambhore and V. G. Anand, *Chem. Rev.*, 2017, **117**, 3420; (*f*) T. Tanaka and A. Osuka, *Chem. Rev.*, 2017, **117**, 2584; (*g*) B. Szyszko, M. J. Białek, E. Pacholska-Dudziak and L. Latos-Grażyński, *Chem. Rev.*, 2017, **117**, 2839; (*h*) S. Dong, T. Y. Gopalakrishna, Y. Han and C. Chi, *Angew. Chem., Int. Ed.*, 2019, **58**, 11742.

13 (*a*) F. Lopez-Garcia, S. Dong, Y. Han, J. J. C. Lee, P. W. Ng and C. Chi, *Org. Lett.*, 2021, **23**, 6382; (*b*) Q. Guo, Z. Fu, L. Zhao and M. Wang, *Angew. Chem., Int. Ed.*, 2014, **53**, 13548.

14 (*a*) V. I. Minkin, *Pure Appl. Chem.*, 1999, **71**, 1919; (*b*) P. George, M. Trachtman, C. W. Bock and A. M. Brett, *Tetrahedron*, 1976, **32**, 1357.

15 (*a*) Y. Segawa, H. Omachi and K. Itami, *Org. Lett.*, 2010, **12**, 2262; (*b*) Y. Segawa, A. Yagi, H. Ito and K. Itami, *Org. Lett.*, 2016, **18**, 1430.

16 CCDC no. for $FEM^{4+}(PF_6^-)_4$ and $CACz^{6+}(SbF_6^-)_6$ is 1991177 and 2177038. The data is provided free of charge by The Cambridge Crystallographic Data Centre (CCDC)†

17 T. Lu and Q. Chen, *Theor. Chem. Acc.*, 2020, **139**, 25.

18 D. Geuenich, K. Hess, F. Köhler and R. Herges, *Chem. Rev.*, 2005, **105**, 3758.

19 (*a*) J. Qian and B. Z. Tang, *Chem*, 2017, **3**, 56; (*b*) G. Feng and B. Liu, *Acc. Chem. Res.*, 2018, **5**, 1404; (*c*) H. Feng, Y. Yuan, J. Xiong, Y. Zheng and B. Z. Tang, *Chem. Soc. Rev.*, 2018, **47**, 7452; (*d*) S. Xu, Y. Duan and B. Liu, *Adv. Mater.*, 2019, 1903530; (*e*) J. Li, J. Wang, H. Li, N. Song, D. Wang and B. Z. Tang, *Chem. Soc. Rev.*, 2020, **49**, 1144.